Supporting Information

In vivo wireless photonic photodynamic therapy

Akshaya Bansal[a,b], Fengyuan Yang[c], Tian Xi[c], Yong Zhang[a,b,1], and John S. Ho[b,c,d,1]

[a]Department of Biomedical Engineering, Faculty of Engineering, National University of Singapore, Singapore 117583, Singapore

[b]Biomedical Institute for Global Health Research and Technology, National University of Singapore, Singapore 117599, Singapore

[c]Department of Electrical and Computer Engineering, Faculty of Engineering, National University of Singapore, Singapore 117583, Singapore

[d]Singapore Institute for Neurotechnology, National University of Singapore, Singapore 117456, Singapore

[1]To whom correspondence should be addressed. Email: biezy@nus.edu.sg or johnho@nus.edu.sg.

Additional Methods

Device assembly. The wireless light delivery device consists a three-turn coil for receiving radio-frequency energy, a rectifier for alternating current to direct current conversion, and two light-emitting diodes (LEDs) (**Fig. S1A**). The LEDs are connected in series with emission spectrum centered at 660 nm and 400 nm respectively, corresponding to the absorption peaks of the photosensitizer Ce6.

The components used were: (1) custom two-sided printed circuit board (PCB) (fabricated through Gold Phoenix Printed Circuit Board), (2) lead-free soldering materials (ChipQuik, SMD291SNL10), (3) Polydimethylsiloxane (PDMS) (Sylgard, 184 silicone elastomer kit), (4) silicone elastomer (World Precision Instruments, Kwik-Sil Adhesive), (5) 0.5pF capacitor (Murata Electronics, GRM0335C1ER50BA01D), (6) 1.2-pF capacitor (Venkel, C0402HQN500-1R2BNP), (7) 10-pF capacitor (Johanson Technology, 250R05L100GV4T), (8) 10-nF capacitor (Murata Electronics, GRM033R61A103KA01D), (9) Schottky diode (Skyworks, SMS7630-061), (10) 36-gauge enameled wire (Belden), (11) red LED chip (Lumex, SML-LX0603SRW-TR) and (12) UV (violet) LED chip (Bivar, SM0603UV-400).
To assemble the device, the PCB was laser cut to the exact size (**Fig. S1B,D**) and components were mounted on using micro-soldering (JBC, NAE-2A) under a microscope (Olympus, SZ61) (**Fig. S1C**,E). The helical coil was formed around the device by wrapping enameled wire three times around the assembled PCB and soldering the two ends on designed pads (**Fig. S1F,G**). Multiple devices were encapsulated in a 3-D printed mold by pouring PDMS (**Fig. S1H**), degassing in a vacuum chamber for one hour, and curing in a forced convection oven (Esco Isotherm) at 70°C for one hour. Encapsulated devices were removed from the mold (**Fig. S1I**) and coated with a thin layer of rapid curing, biocompatible silicone (Kwik-Sil, WPI) to enhance electrical isolation and surface smoothness (**Fig. S1J**).

Light emission characteristics of the LEDs. Light emission from red (Lumex, SML-LX0603SRW-TR) and violet (Bivar, SM0603UV-400) LEDs was measured by directly driving the device through a DC power supply (Keysight, E3631A). The emission spectrum was measured using a high-resolution spectrometer (OceanOptics, HR2000+) and recorded using analysis software (Ocean Optics SpectraSuite). The

radiant power was measured for the red and violet LEDs separately using an optical power meter (Newport, 2935-C) over a range of driving currents (0.1 mA to 20 mA) calibrated for 660 nm and 400 nm light, respectively (**Fig. S2**).

Device biosafety. Device biosafety *in vitro* was evaluated by culturing tumor (MB49, bladder cancer) and non-tumor (HEK293T, human embryonic kidney) cells on a silicone encapsulated device followed by Calcein/Propidium iodide (PI) staining to ascertain the percentage of live and dead cells (**Fig. S3A,B**). Non-fluorescent Calcein is cell permeant and is converted to a highly fluorescent form by the esterase activity of live cells, which are detected by green fluorescence (ex/em 488nm/520nm). In contrast, PI is non-permeant and binds to nucleic acids only when the cell membrane is compromised, producing bright red fluorescence (ex/em 488nm/635nm).

For evaluating *in vivo* biosafety in **Fig. S3C-E**, mice were implanted and monitored for 3 weeks, after which the devices were explanted with adjacent tissue and blood samples obtained. The blood samples were spun down to obtain plasma, and ELISA performed to determine the concentration of C3 complement and Fibrinogen (Mouse complement C3 ELISA assay, abcam, cat. no. ab157711 and Fibrinogen mouse ELISA kit, abcam, cat. no. ab108844). Capsules surrounding the device was fixed by formalin and stained for alpha- smooth muscle actin, a marker for myofibroblasta. Tissues adjacent to the device were cryosectioned and H&E stained. As controls, blood and tissue samples were extracted from non-implanted mice and similarly processed.

Long-term device functionality. To test long-term functionality, devices were submerged in phosphate-buffered saline (PBS) and cell culture solution (n=9) individually in safe-lock tubes (Eppendorf) over 220 days. The devices were placed in an incubator with temperature maintained at 37°C. The devices were tested weekly by wirelessly powering the devices through the tubes and visually checking inspecting the device for light emission (**Fig. S3F**).

Light scattering experiments. To measure the light distribution around the device in a tissue-like environment, we synthesized a 3-mm thick optical tissue phantom using PDMS (Sylgard 184) and aluminium oxide (Sigma Aldrich), previously shown to reproduce the optical scattering properties of skin tissue as described in Ref. (1). The

device placed in a 2-mm diameter hold punctured in the slab with either a red (660 nm) or violet (400 nm) LED oriented such that the emission direction is parallel to the phantom surface. The device was wirelessly activated and light distribution on the surface of the phantom imaged using a microscope (Olympus, SZ61) and camera (Olympus, DP22) in a dark environment (**Fig. S4**). The light intensity was controlled by the current driving the LED, measured by a multimeter (Keysight, U1242C).

Light transport simulations. The Monte Carlo method was used to simulate photon transport in tumor tissue using the MATLAB software package mcxyz (http://omlc.org/software/mc/mcxyz/). The light source was modeled as a uniform beam with an aperture size of 1 mm. The source was placed in the center of the simulation domain (2 cm cube, 0.1 mm bin size, 200 bins in each dimension) consisting of homogenous tissue. Tissue optical properties were set using scattering and absorption parameters for tumor tissue in Ref. (2) with varying blood volume fraction (**Fig. S5**). Simulation time was set to 10 min. Images show simulated irradiance cross-sections for each bin while contours show cross-sections filtered (2D Gaussian, σ=5 bins) for smoothness.

ROS production in solution and in cells. For direct ROS production studies, Chlorin e6 (Ce6, trisodium salt, Precision Technologies, Pte Ltd) was prepared at 0, 2, 5 and 8 μM concentrations in deionised (DI) water. Solutions were transferred to transparent cuvettes (1.5 ml/cuvette, n=3 for each concentration) and SOSG dye (3 μl, singlet oxygen sensor green, ThermoFisher Scientific, Cat. no. S36002) was added. Cuvettes were illuminated with the device emitting violet light, red light, or both, either wirelessly or by directly driving the LEDs with a DC power supply. At each time point (0, 20, and 40 min), samples (100 μl) were drawn from each cuvette and transferred to an opaque 96 well plate (Corning).

Initial ROS production studies were carried out using devices directly wired to a DC power supply for ease of control of the radiant power level (optical 0.4 to 4.5mW). After ROS production was established, wireless devices emitting red light, violet light, or both were used to irradiate 5 μM Ce6 solution at various RF power levels (RF 90 to 290 mW) by placing a near-field transmitter in close proximity to the device. **Fig. S10** shows that wireless powering at RF 190 mW results in ROS

production comparable to wired devices directly driven at radiant powers of 3.3 to 4.5 mW emitting violet light or both red and violet light. Devices emitting only red light required higher power (RF 290 mW) to achieve ROS production comparable to wired devices (optical 1.3 mW). Based on these studies, the RF power level for the near-field configuration was set to about 200 mW for subsequent studies.

For cellular ROS production studies, MB49 murine bladder cancer cells (obtained from American type culture collection (ATCC)) were cultured in a 24 well plate (Costar) and incubated with 5 μM Ce6 overnight. Cells were washed the next day, stained with Image-iT LIVE Reactive Oxygen Species (ROS) (Molecular Probes, OR, USA), and irradiated for 20 min using violet, red or dual light emitting devices either wirelessly or by directly driving the LEDs with a DC power supply (**Fig. S8-9**). The samples were then washed three times with PBS (phosphate buffered saline) and imaged using a confocal laser-scanning microscope (Nikon C1 Confocal, Nikon, Tokyo, Japan). Green fluorescence indicates ROS production (488/540 ex/em). Cells were also counterstained with DAPI. All images were taken using the same gain and pixel dwell (30 μs) values.

Surface heating due to RF and laser exposure. Thermal effects on the skin due to radio-frequency (RF) and laser exposure in **Fig. S13** were measured in anesthetized tumor-bearing mice. For RF exposure, the near-field loop transmitter was placed directly above the tumor site with the RF output power set to 200 mW. For laser exposure, the spot size was adjusted to illuminate the entire tumor volume and the irradiance set to 100 mW/cm^2. Measurements were acquired at 1 min intervals by briefly turning off the exposure source and placing a thermocouple (Omega Engineering) on the skin surface.

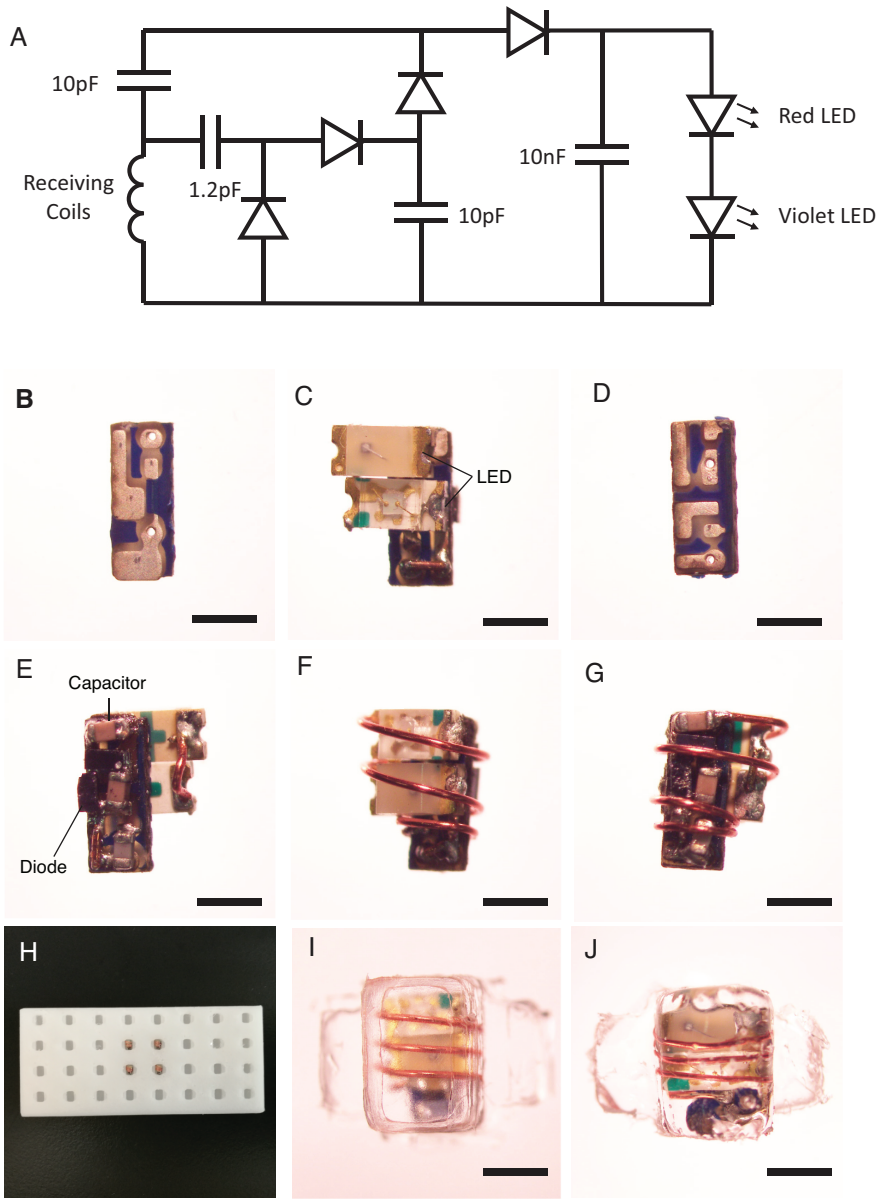

Figure S1. Device assembly. (A) Circuit schematic of the device. (B-E) Components were mounted on a two-sided printed-circuit board (PCB) and (F,G) enameled wire wrapped around the device to form a three-turn helical coil. (H) The completed circuit board was placed in a 3D-printed mold and (I,J) encapsulated in transparent silicone. Scale bar, 1 mm.

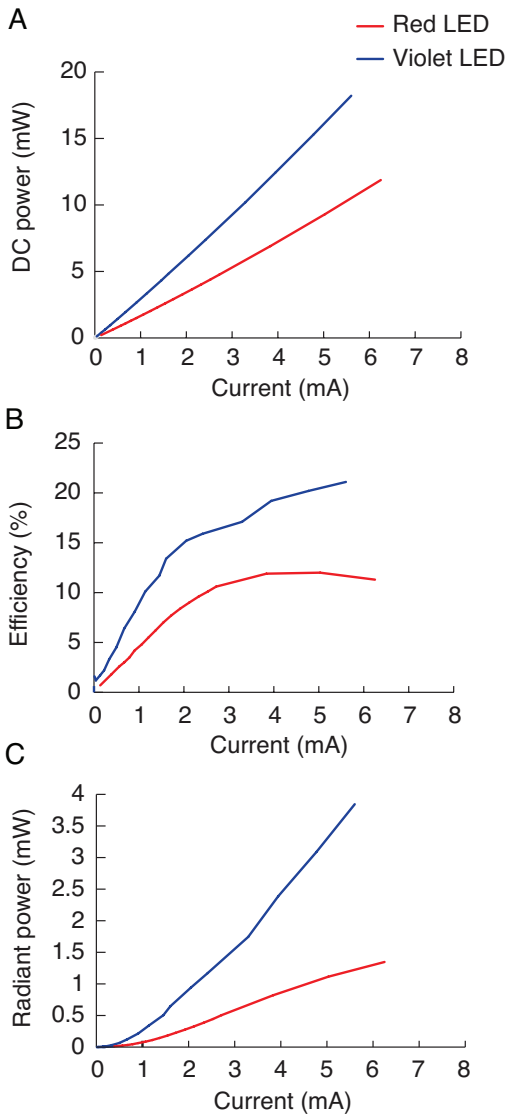

Figure S2. Characterization of LEDs. (A) DC power dissipated by the violet and red LED, (B) efficiency of direct-current power to light conversion, and (C) optical radiant power emitted as a function of direct current.

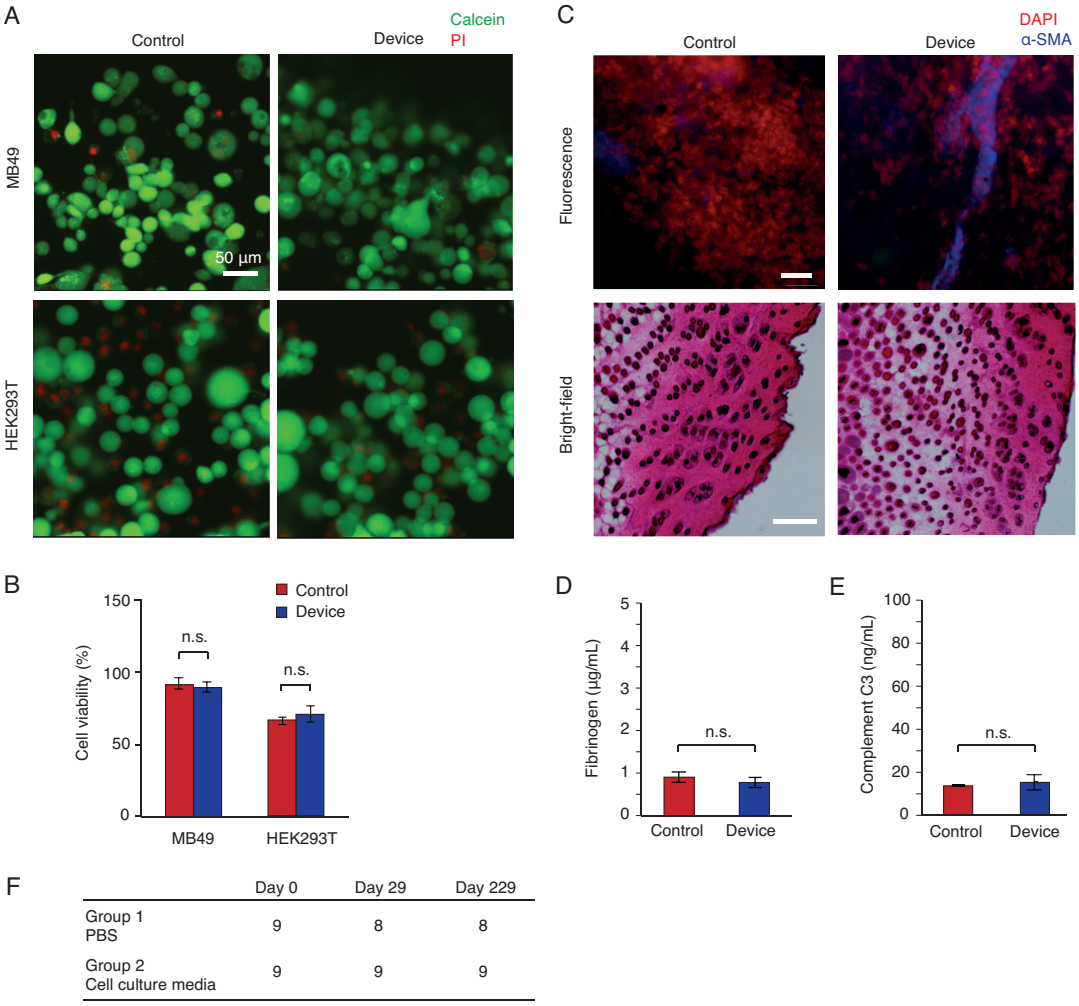

F

	Day 0	Day 29	Day 229
Group 1 PBS	9	8	8
Group 2 Cell culture media	9	9	9

Figure S3. Device biosafety. (A) Confocal fluorescence microscopy images of MB49 (cancer) and HEK293T (non-cancer) cells grown on the device for 3 days. Green fluorescence (calcein ex/em 488/520 nm) indicates live cells and red fluorescence (PI, ex/em 488/635 nm) dead cells. Control cells were incubated without the device. (B) Viability analysis of MB49 and HEK293T cells. (C) Histological analyses of tissues around device implanted for 3 weeks. Tissues were stained for alpha smooth muscle actin (α-SMA) in addition to H&E staining (scale bar 100µm). Control tissues were obtained from non-implanted mice. (D-E) Fibrinogen and Complement C3 concentration in plasma from implanted (device) and non-implanted mice (control) measured by ELISA. (F) Number of functional devices following submersion in phosphate-buffered solution (PBS) and cell culture media at 37°C. Graphs show mean ± s.d. ($n=3$ per group).

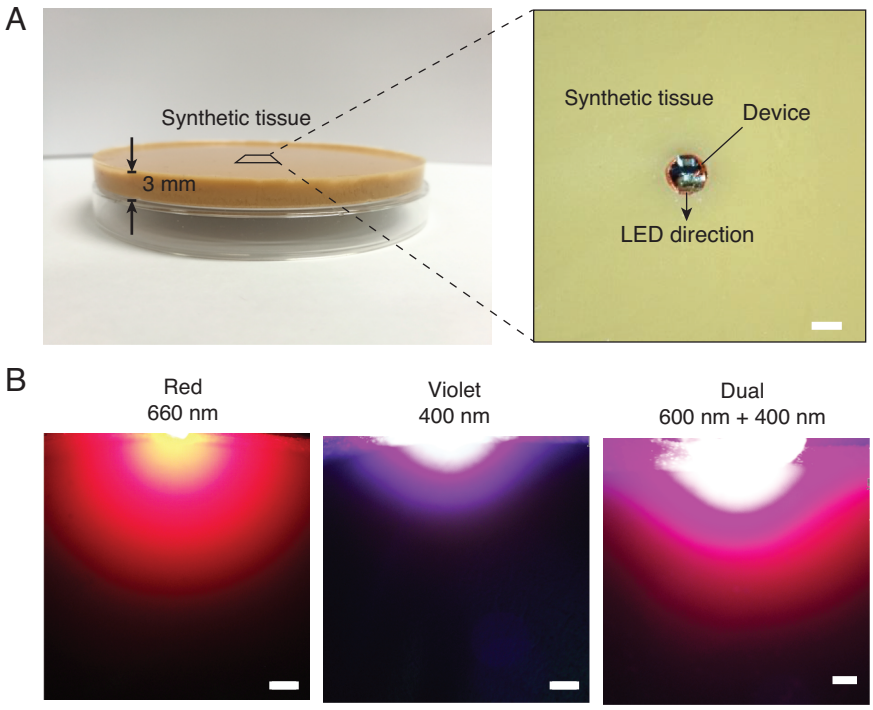

Figure S4. Light distribution in synthetic tissue. (A) Image of the synthetic tissue slab and (inset) top view with device inserted into the slab with LED direction parallel to the surface. (B) Light distribution images with device placed at edge of the slab (bottom). All LEDs are driven at 2 mA. Scale bar, 2 mm.

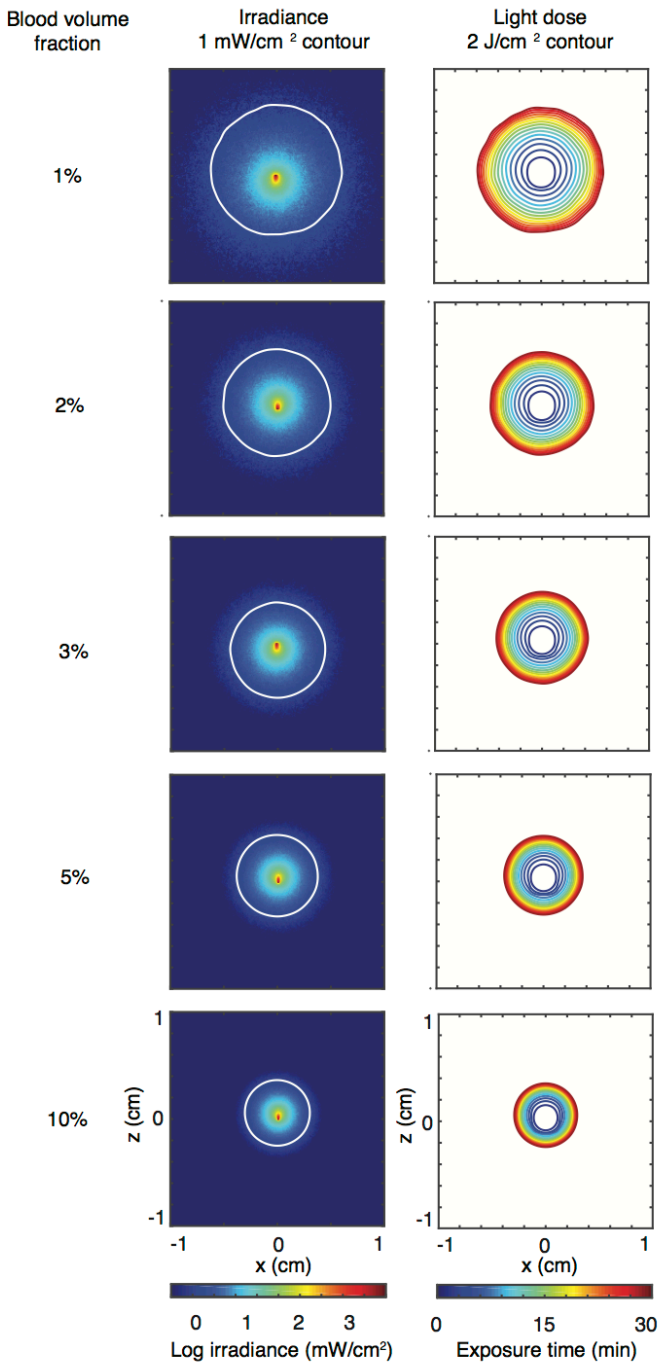

Figure S5. Light transport simulations. Optical irradiance around the device (white line shows 1 mW/mm^2 contour) and light dose contours (2 J/mm^2 after 1 to 30 min of exposure) for device emitting in homogenous tumor-like tissue with blood volume fraction varying from 1% to 10%. The total radiant power emitted by the device is 1 mW.

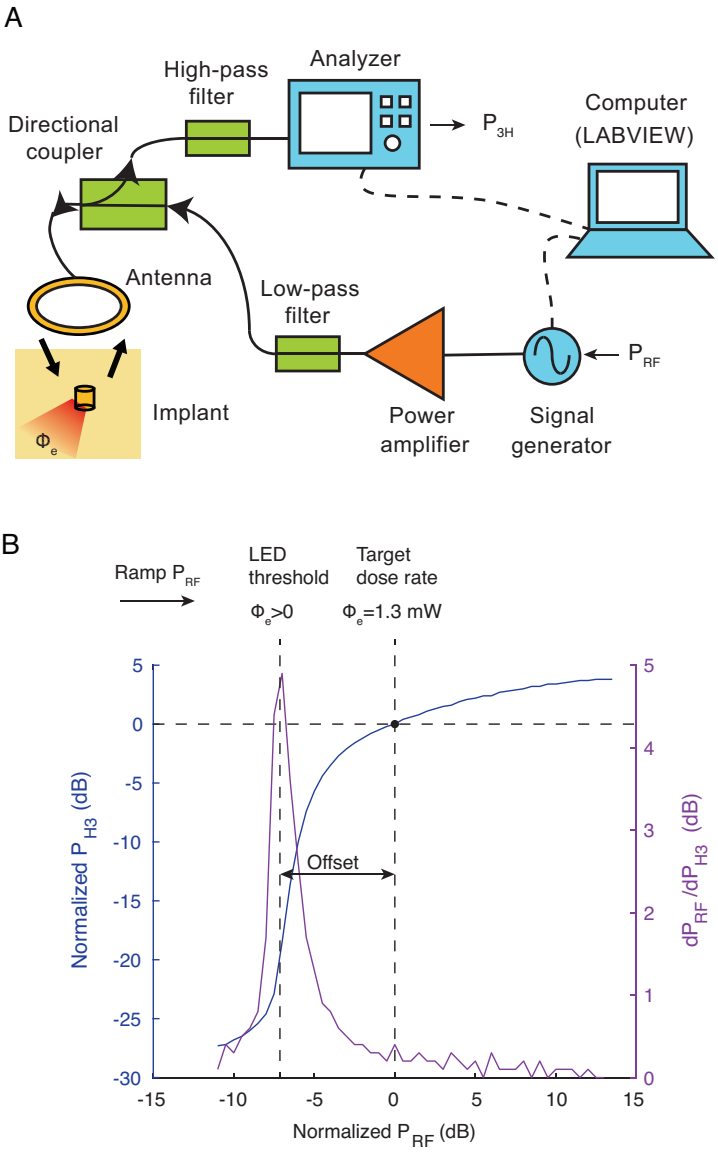

Figure S6. Wireless dosimetry by harmonic detection. (A) Schematic of the wireless dosimetry system. The signal generator controls P_{RF}, the radio-frequency power transmitted, while the spectrum analyzer measures the power of the backscattered third harmonic P_{H3}. (B) P_{H3} as a function of P_{RF} normalized to the respective power levels at the Φ_e=1.3 mW operating point. The derivative dP_{H3}/dP_{RF} is also shown. The harmonic power abruptly increases around the LED threshold, from which the target dose rate can established by a predetermined offset.

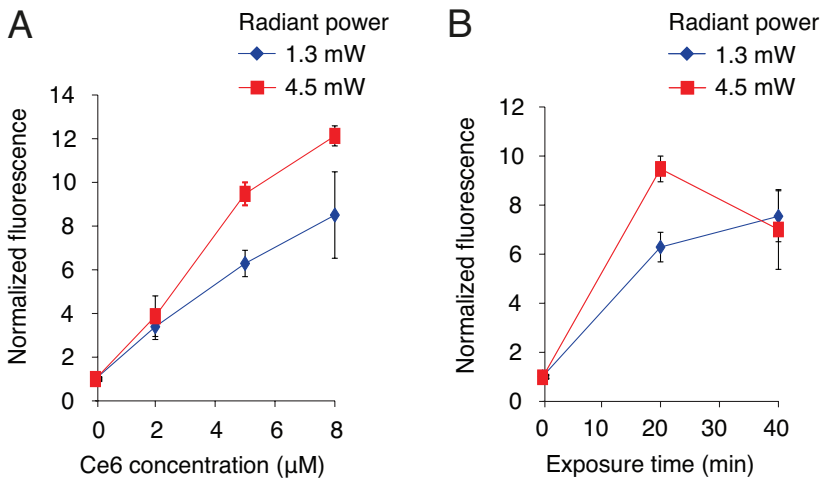

Figure S7. Ce6 ROS production under wireless device illumination. (A) Normalised ROS sensor fluorescence in solution for varying concentrations (0, 2, 5 and 8 µM) of Ce6 after 20 min of irradiation at 1.3 and 4.5 mW radiant power. (B) Normalised ROS sensor fluorescence as a function of light exposure time in 5 µM Ce6 solution at 1.3 and 4.5 mW radiant power. Graphs show mean ± s.d. (*n=3* per group).

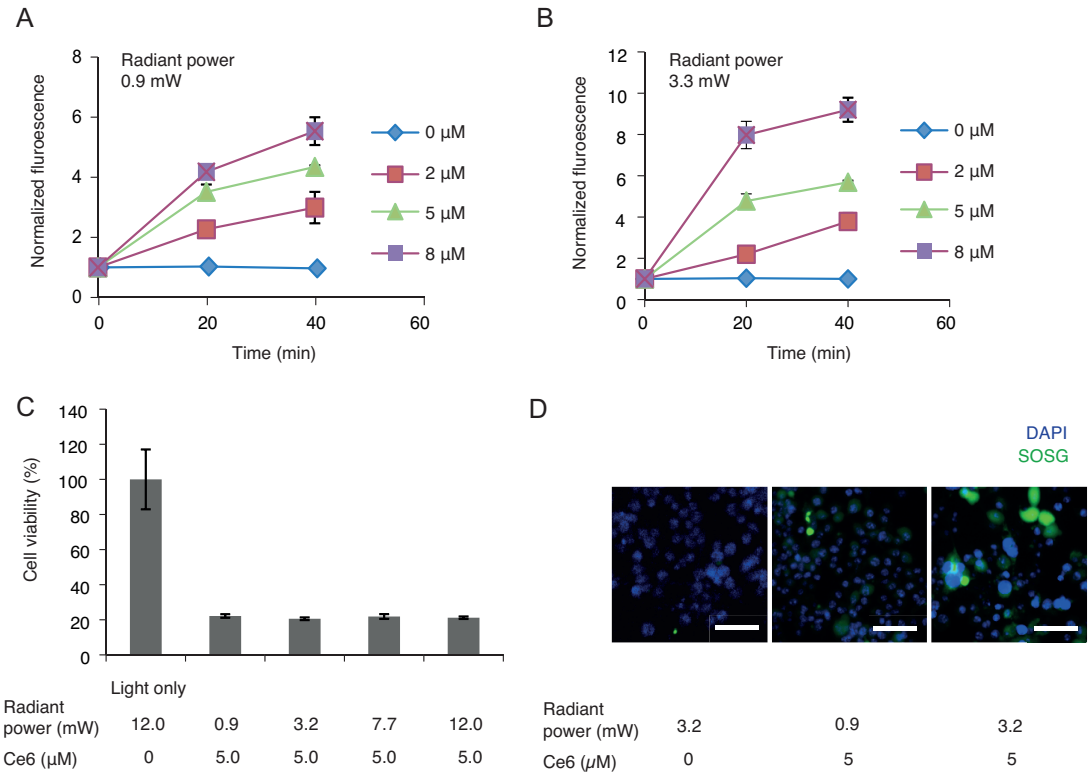

Figure S8. *In vitro* PDT using violet light emitting device. (A,B) Normalised ROS production from Ce6 (Clorin e6) at varying concentrations (0, 2, 5 and 8 µM) and exposure to violet light from wired light emitting devices at different intensities, corresponding to radiant powers of (A) 0.9 mW and (B) 3.3 mW. (C) MTS assay to show change in viability of MB49 bladder carcinoma cells following PDT. Controls include untreated cells, cells exposed to Ce6 alone and light alone. (D) ROS production (green fluorescence) in live cells following irradiation of cells. Blue fluorescence indicates nuclei. Untreated cells serve as the control group. Graphs show mean ± s.d. ($n=3$ per group).

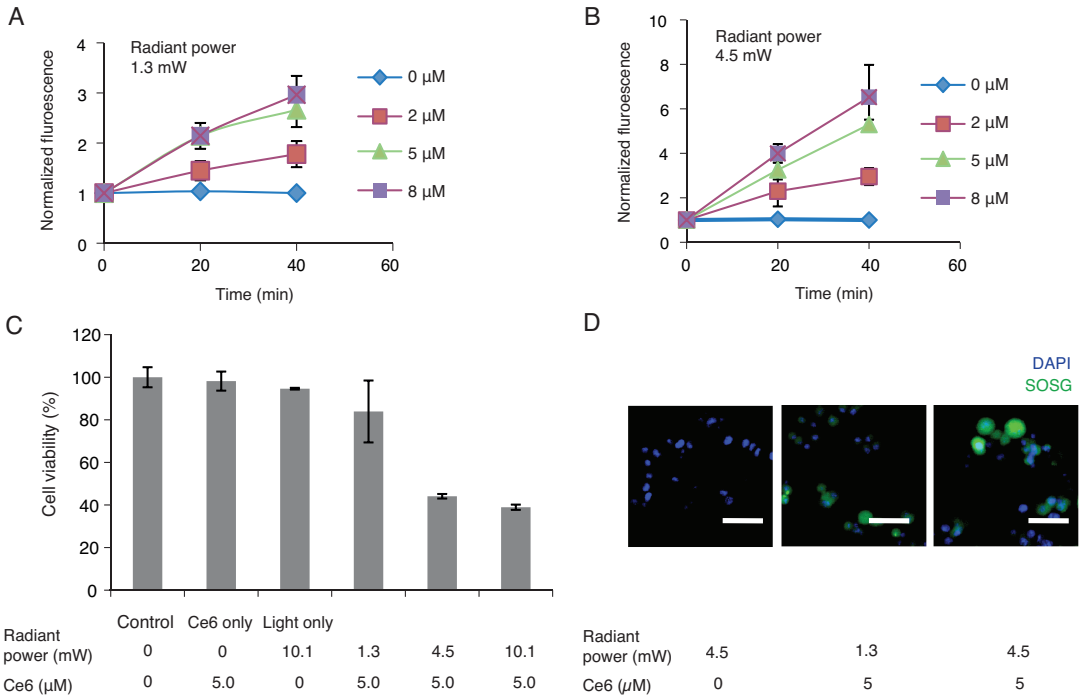

Figure S9. *In vitro* PDT using red light emitting device. (A,B) Normalised ROS production from Ce6 (Chlorin e6) at varying concentrations (0, 2, 5 and 8 µM) and exposure to red light from wired light emitting devices at different intensities, corresponding to radiant powers of (A) 1.3 mW and (B) 4.5 mW. (C) MTS assay to show change of MB49 bladder carcinoma cells following PDT. Controls include untreated cells, cells exposed to Ce6 alone and light alone. (D) ROS production (green fluorescence) in live cells following irradiation cells. Blue fluorescence indicates nuclei. Untreated cells serve as the control group. Graphs show mean ± s.d. (*n=3* per group).

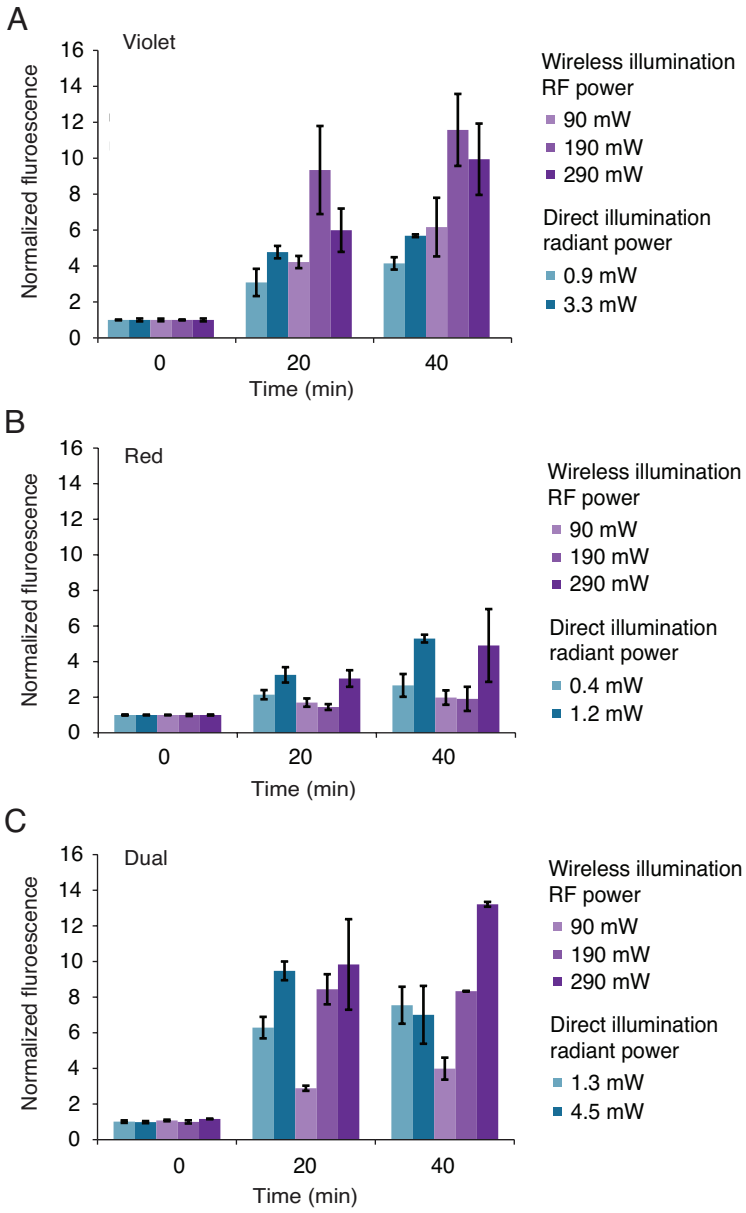

Figure S10. ROS production in solution under direct and wireless illumination. (A-C) Normalized fluorescence of SOSG following 0, 20, and 40 min irradiation with (A) violet (400 nm), (B) red (660 nm), or (C) both light-emitting devices. Ce6 concentration was 5 μM. Direct illumination levels consist of LED radiant power controlled by wired power supply, while wireless illumination levels consist of output radio-frequency (RF) power in the near-field wireless powering configuration. Graphs show mean ± s.d. (*n=3* per group).

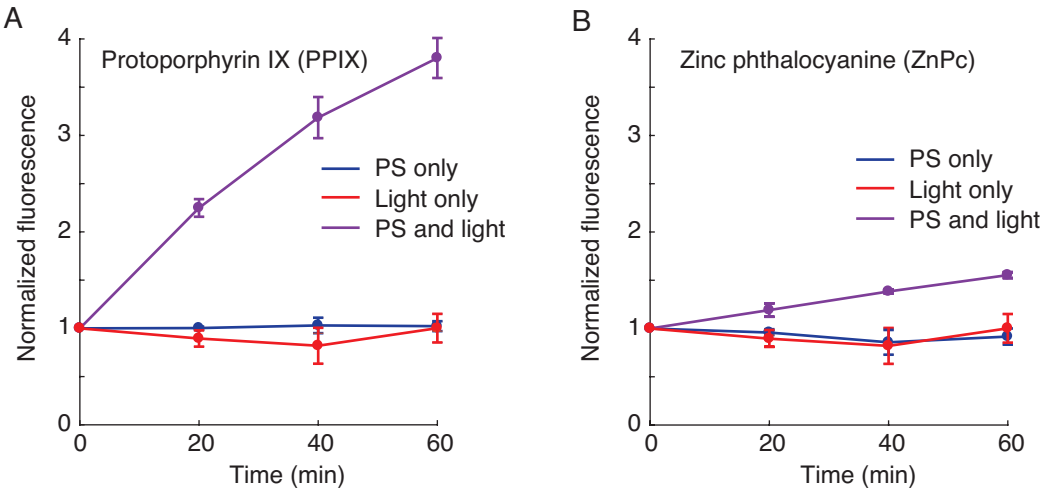

Figure S11. Compatibility with other photosensitizers. ROS production from (A) protoporphyrin IX (PPIX) and (B) zinc phthalocyanine (ZnPc). The photosensitizers are irradiated with dual light emitting wireless device at 1.3 mW radiant power. Graphs show mean ± s.d. (*n=3* per group).

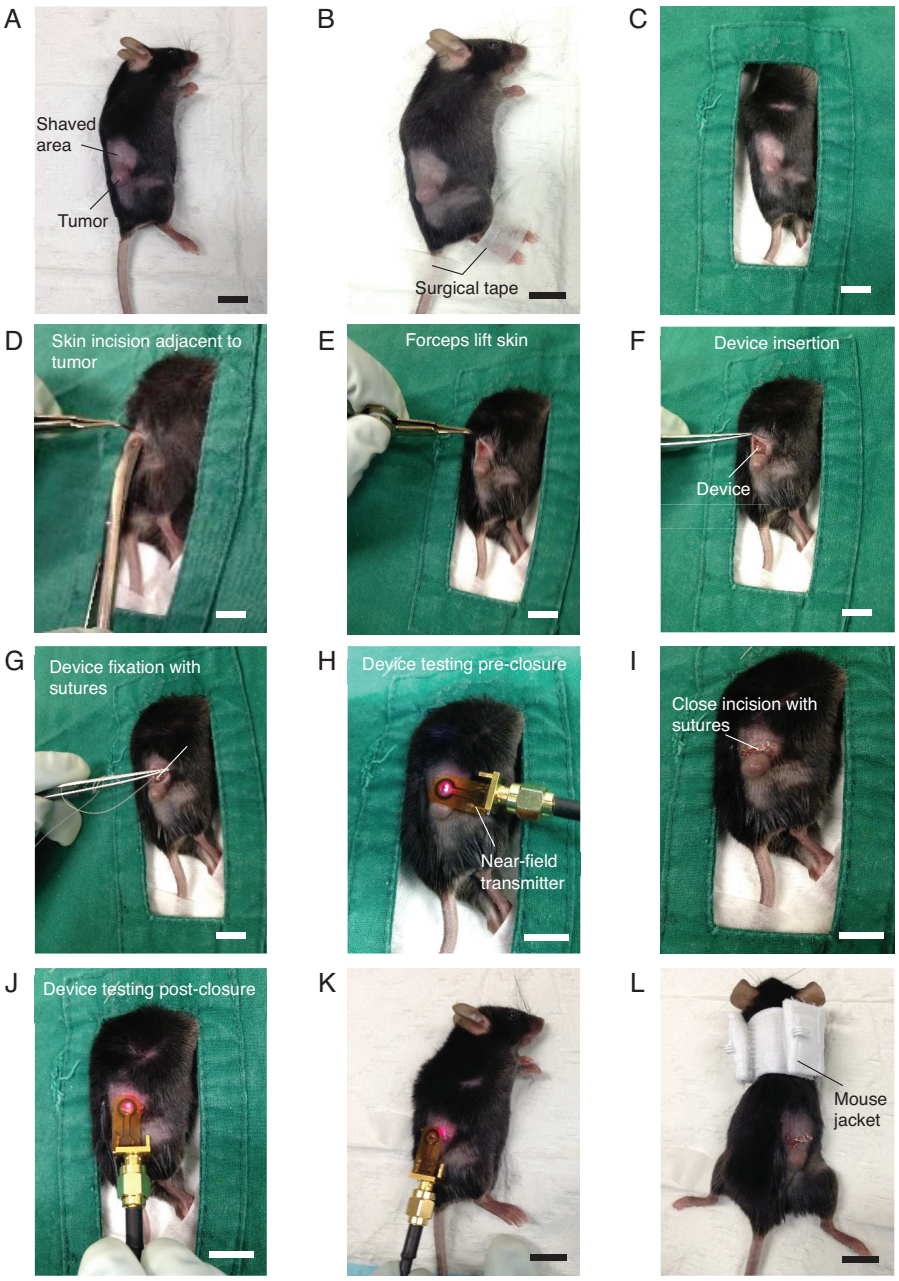

Figure S12. Surgical procedure for implantation of the wireless photonic device. (A) The tumor area is shaved and (B) the hind legs and tail fixated with surgical tape. (C) The body is covered by a surgical drape and (D) an incision is made adjacent to the tumor. (E) The skin is gently lifted, (F) allowing the device to be inserted. (G) The device is fixed in place by suturing flaps to the skin. (H) The device is tested by visually checking for light emission during wireless powering. (I) The incision is closed by suturing and (J,K) the device tested again by wireless powering over the skin. (L) Mice were placed in jackets for 3-5 days after implantation to protect the surgical site. Scale bar, 1 cm.

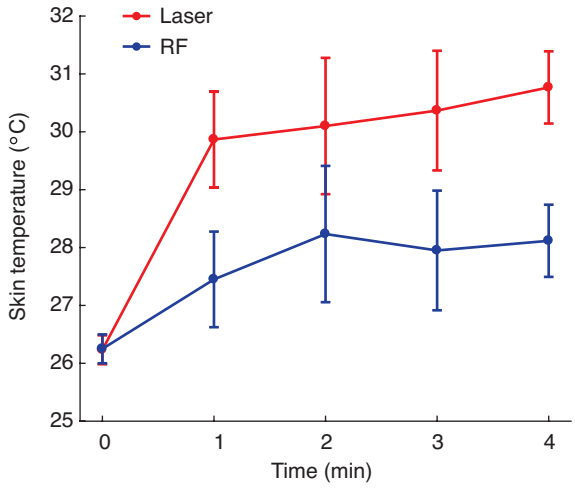

Figure S13. Thermal effect of laser and radio-frequency (RF) field exposure. Skin temperature as a function of exposure time in anesthetized mice. The temperature measured by a thermocouple in 1 min intervals with the illumination briefly turned off. Laser output power, 100 mW/cm^2; RF output power, 200 mW. Graphs show mean ± s.d. (*n=3* technical trials).

Additional References

1. Lualdi M, Colombo A, Farina B, Tomatis S, & Marchesini R (2001) A phantom with tissue-like optical properties in the visible and near infrared for use in photomedicine. *Lasers Surg. Med.* 28(3):237-243.
2. Jacques SL (2013) Optical properties of biological tissues: a review. *Phys. Med. Biol.* 58(11):R37.